**EDGE ARTICLE**

Check for updates

# Crosslinker nanocarrier-based intratumoral delivery for protein complex mapping in mitochondria of live tumor-bearing mice

Yuwan Chen,†[ab] Wenxin Fu,†[ad] Baofu Ma,[ab] Xinwei Li,[ac] Wen Zhou,[ab] Zhen Liang,[a] Kaiguang Yang, [ID] *[a] Lihua Zhang [ID] *[a] and Yukui Zhang[a]

Mitochondria, the powerhouses of the cell, are central to tumor initiation and growth, yet their protein interactions in living tumors remain poorly understood. Although crosslinking mass spectrometry (XL-MS) has revealed protein conformations and interactions in cultured cells and isolated tissues, its *in vivo* application remains limited by poor crosslinker delivery. Here, we present an approach that uses intratumoral injection of crosslinker-loaded nanoparticles in xenografted mice to enable *in vivo* DSS crosslinking of tumor mitochondria, thereby facilitating XL-MS-based analysis of mitochondrial protein complexes. We identified 2368 crosslinked peptides from 654 mitochondrial proteins, covering 58% of the human mitochondrial proteome. Among these, 549 crosslinked peptides were mapped to proteins involved in thermogenesis, ribosome function, and branched-chain amino acid degradation—metabolic pathways closely linked to tumor progression. Structural concordance was high (92%) with PDB and AlphaFold models, and complementary conformational insights were obtained, including previously missing data on the DAPIT subunit of ATP synthase, thus complementing cryo-electron microscopy (cryo-EM) structures. We further mapped 217 mitochondrial PPIs, including 146 not annotated in STRING, highlighting the influence of the tumor microenvironment on protein interactions *in vivo* and providing valuable insights into tumor biology.

## Introduction

Mitochondria play a critical role in regulating cellular energy and metabolism. One of their key functions is to synthesize ATP through oxidative phosphorylation to meet cellular energy demands.[1] Cancer cells exhibit abnormal proliferation, division, and apoptosis,[2,3] accompanied by abnormal energy requirements, and grow in a particularly complex microenvironment[4] composed of various cellular components and the tumor stroma. This tumor microenvironment profoundly influences cancer signaling pathways, as well as tumor invasion and metastasis. Mitochondria are also essential for sustaining the growth and survival of cancer cells. Therefore, profiling mitochondrial protein conformation and the interactome in live tumors, where the native microenvironment is preserved, provides valuable insights into tumor protein phenotypes,

which will aid in the identification of potential biomarkers and therapeutic targets.

Crosslinking mass spectrometry (XL-MS) has been widely employed to analyze mitochondrial protein conformations and protein−protein interactions (PPIs) in isolated mitochondria.[5–8] More recently, *in vivo* XL-MS with nanocarriers to deliver crosslinkers to the target suborganelle was developed to obtain such information in living cells.[9,10] However, studies in live tumors remain lacking, owing to challenges arising from non-targeted crosslinkers with high reactivity and the difficulty of traversing multiple biological barriers to reach the specific subcellular organelles within tumors. Within the tumor microenvironment, amine-containing components will quench crosslinker reactive functional groups.

Herein, we developed positively charged PLGA-nanocarriers that target mitochondria *via* electrostatic interactions and deliver DSS into HepG2 cells, enabling *in situ* MS analysis of mitochondrial protein structures and interactions under culture conditions.[9,10] Taking advantage of PLGA nanoparticles, which protect biomolecules from immune clearance and metabolic degradation and enable the delivery of drugs, genes, and vaccines *in vivo*,[11] we further employed positively charged PLGA nanoparticles to load and deliver DSS into mitochondria *via* intratumoral injection in tumor-bearing mice. Following *in vivo* crosslinking, tumors were isolated and processed using the

[a]State Key Laboratory of Medical Proteomics, National Chromatographic R. & A. Center, Dalian Institute of Chemical Physics, Chinese Academy of Sciences, Dalian 116023, China. E-mail: lihuazhang@dicp.ac.cn; yangkaiguang@dicp.ac.cn

[b]University of Chinese Academy of Sciences, Beijing 100049, China

[c]School of Chemistry, Dalian University of Technology, Dalian 116024, China

[d]Research Center for Analytical Sciences, Northeastern University, Shenyang 110819, China

† Y. C. and W. F. contributed equally.

i-FASP method[12] for protein complex extraction and digestion. Given the complexity of liver cancer tissue and the low abundance of crosslinked peptides, reversed-phase liquid chromatography (RPLC) fractionation was employed to reduce sample complexity. Finally, the identified crosslinked peptides were used to map mitochondrial protein conformations and interactions (Fig. 1).

## Results and discussion

### Mitochondrial protein complex mapping in live tumor-bearing mice *via* nanocarrier-delivered crosslinking

In our previous study, engineered nanoparticles were successfully fabricated to deliver crosslinkers to mitochondria, enabling crosslinking in the target mitochondria of living HepG2 cells (CD-MS method).[9] Herein, we applied the CD-MS method, by which DSS was efficiently delivered to mitochondria in HepG2 xenograft tumors within 6 h after intratumoral injection of positively charged PLGA nanoparticles (DSS-DDAB@PLGA/Kolliphor EL NPs). Subsequently, crosslinked HepG2 tumors were isolated, and protein complexes were further extracted and digested *via* the i-FASP method.[12] Finally, we identified 2368 unique crosslinked peptides in 654 proteins, which corresponded to 2470 crosslinking sites (crosslinks) and 58% of the human mitochondrial proteome (SI Fig. 1). Non-uniform intratumoral NP distribution can limit spatial coverage and bias crosslink-derived interactions toward regions with higher NP exposure. However, our nanoparticles are positively charged, a feature expected to facilitate transport across tumour barriers; moreover, once internalized, the 70DSS-DDAB@PLGA/Kolliphor EL NPs preferentially target mitochondria as shown in our previous work. Despite these constraints, the depth of mitochondrial crosslinking achieved and the comparatively low stromal density of the HepG2 xenograft support the biological interpretability of the dataset. In addition, the copy numbers of the crosslinked proteins spanned a range of five orders of magnitude, reflecting their expression abundances (SI Fig. 2).[13] These data demonstrated that our

approach could label mitochondrial proteins of HepG2 cells in live tumor-bearing mice.

For PPIs in HepG2 xenograft tumors, we totally identified 212 inter-crosslinked peptides, corresponding to 217 PPI pairs. These interactions were mapped according to the subcellular localization of mitochondrial proteins across all four mitochondrial subregions (Fig. 2a), indicating that the nanocarrier-based crosslinker targeted delivery strategy effectively captures PPIs within mitochondria of HepG2 tumor cells. The STRING score was used to evaluate the evidence support of identified PPIs.[14] Among the 217 detected PPIs, 32.72% (71/217) were previously reported in the STRING database (SI Fig. 3), of which



Fig. 2 The spatial distribution of PPIs identified from crosslinked peptides and GO biological process (GOBP) analysis of novel PPIs. (a) Based on SubMitoLocalization data from MitoCarta3, mitochondrial crosslinked peptides detected across all fractions were categorized and displayed according to the sub-mitochondrial localization of the interacting proteins: outer membrane (MOM), intermembrane space (IMS), inner membrane (MIM), and matrix. In the network, nodes represent individual proteins, and lines represent crosslinks between them. Red lines indicate previously unreported interactions. (b) GO biological process (GOBP) analysis of the newly identified, unannotated PPIs, grouped by functional category.
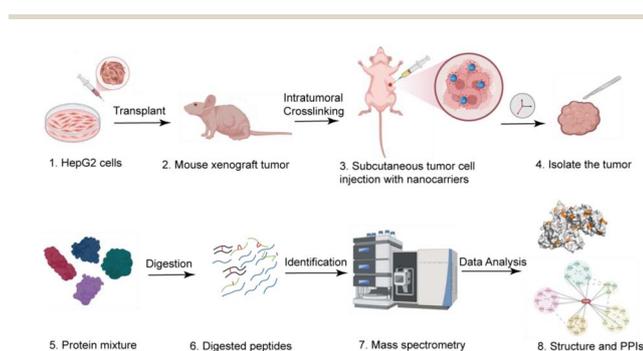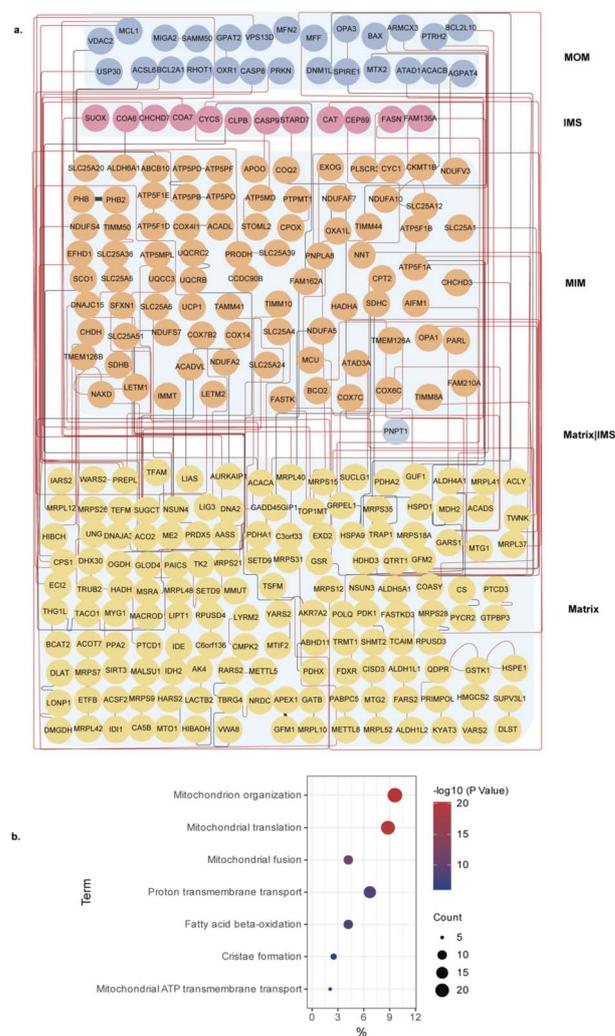


Fig. 1 Identification of mitochondrial protein interactions and conformational information in tumor-bearing mice. A HepG2 xenograft mouse model was established. Crosslinking was performed using DSS intratumorally delivered *via* nanocarriers. The crosslinked tumors were isolated, followed by protein complex extraction, digestion, and nano-RPLC–MS/MS analysis, to decipher *in vivo* protein conformation and PPI.

28.1% (20/71) had high confidence scores (>0.7) (SI Fig. 3). Notably, 67.28% (146/217) of the PPIs were not annotated in STRING (Fig. 2a, red lines) (1% FDR). This would be caused by the fact that most PPI data in the STRING database come from standard culture conditions, whereas our study detected mitochondrial protein crosslinking in the living tumor microenvironment.

GOBP analysis revealed that the crosslinked proteins involved in these PPIs were predominantly enriched in mitochondrial organization (Fig. 2b), which is closely related to mitochondrial morphological transformations. Our *in vivo* crosslinking method (*via* mitochondrial localization in living tumors) maximally preserves native protein conformations and interactions, enabling detection of dynamic/transient interactions that are difficult to capture in traditional cell cultures or isolated mitochondria. Additionally, the results indicate that most identified proteins are involved in mitochondrial translation, fusion, and proton transmembrane transport (Fig. 2b). Considering the broader context of metabolic modulators of cancer, effects on mitochondrial translation are frequently associated with mitochondrial diseases and reduced activity of multiple respiratory chain (RC) enzymes.[15] Of the 217 PPIs identified in this study, ten overlapped with the 153 interactions previously mapped using DSS in HepG2 mitochondria[9] (SI Fig. 4), including the HSPD1–SND1 interaction, which is not annotated in STRING. Notably, a previous study[16] reported that ELISA screening of antibodies against 26 phage-expressed proteins in sera from hepatocellular carcinoma (HCC) patients, chronic hepatitis patients, and healthy controls identified HSPD1 and SND1 as significantly different between groups ($P < 0.05$), supporting their diagnostic potential. These findings suggest that the interaction between HSPD1 and SND1 may play an important, yet previously overlooked, role in liver disease. In addition, OPA1 and MFN2 are well-established regulators of mitochondrial fusion and are implicated in autosomal dominant optic atrophy and Charcot–Marie–Tooth disease type 2As.[17] The interactions we observed between MRPL37 and OPA1, and between MRPL37 and MFN2, raise the possibility that the mitochondrial large ribosomal subunit protein MRPL37 may be functionally connected to mitochondrial fusion, although further validation is required.

## Protein conformation and interactome in thermogenesis from HepG2 tumor cells

KEGG pathway analysis[18] of the 654 identified crosslinked proteins revealed enrichment of 80 proteins in thermogenesis as the second-ranked pathway, which is closely associated with tumor-related abnormal thermal metabolism, elevated temperatures, and mitochondrial energy conversion (SI Fig. 5). To further characterize these proteins, we mapped crosslinked sites onto experimental PDB structures and AlphaFold prediction models. Among these proteins, 179 crosslinked peptides were assigned to 46 oxidative phosphorylation (OXPHOS) proteins spanning the electron transport chain (ETC, complexes I–IV) (Fig. 3a), 145 crosslinked peptides to 14 proteins of ATP
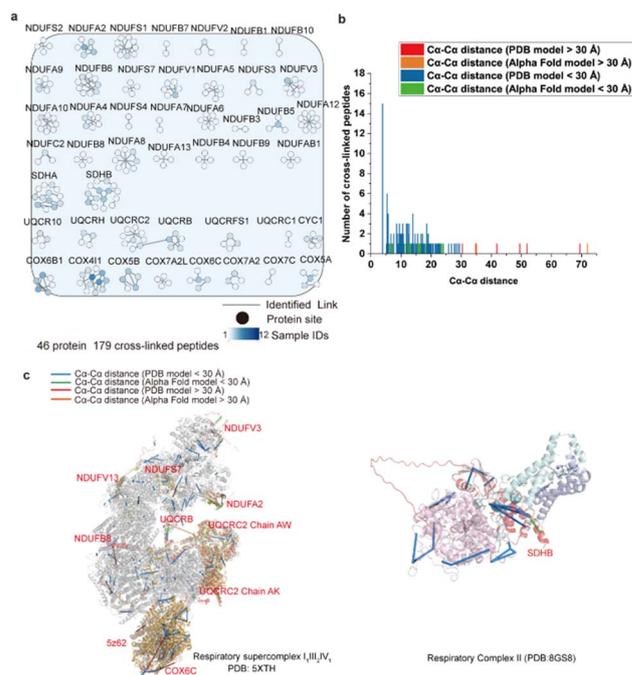


Fig. 3 Crosslinked peptides of OXPHOS proteins. (a) Crosslinked peptides related to OXPHOS proteins were selected from SI Fig. 1 and displayed individually. In the network, nodes represent proteins and lines represent identified crosslinks between them. Node colors indicate the number of samples in which each protein interaction was observed. (b) Histograms showing the length distribution of all distance restraints on protein structures (from (c)) after docking. Crosslinks within 30 Å are shown in blue (PDB model) or green (AlphaFold model), while those exceeding 30 Å are shown in red (PDB) or orange (AlphaFold). (c) The detected crosslinked sites were mapped on the SCI$_1$III$_2$IV$_1$ structure (PDB codes: 5Z62 & 5XTH) and complex II structure (PDB code: 8GS8). Crosslinked peptides were positioned on the Cα–Cα distances of subunit residues. The AlphaFold model aligned with the supercomplex is shown in red (see the Methods section for details), with crosslinks positioned on Cα–Cα distances within its subunit residues. Subunits of 5XTH are shown in grey, 5Z62 in orange, and 8GS8 in different colors.

synthase (complex V) (Fig. 4a), and 29 peptides to 18 thermogenic metabolism-related proteins (SI Fig. 6).

First, we mapped the crosslinked peptides to 46 oxidative phosphorylation proteins using experimental PDB structures and AlphaFold prediction models. In addition to the four crosslinked peptides identified for NDUFV3 (for which no structural data are available in either the PDB or AlphaFold), we identified 15 crosslinked peptide pairs involving 10 subunits (NDUFA13, NDUFS7, NDUFA2, NDUFV3, NDUFB8, SDHB, UQCRB, UQCRC2, COX6C, and COX7A2L) spanning complexes I–IV. These crosslink sites are located in regions that are unresolved in the PDB structure of the human supercomplex CI$_1$-III$_2$IV$_1$ (SCI$_1$III$_2$IV$_1$)[19] and complex II. Of these, 13 pairs were consistent with AlphaFold-predicted structural models. Notably, an inter-crosslinked peptide linking Lys-4 of UQCRB and Lys-92 of UQCRC2 was detected within complex III. Due to the absence of structural data for Lys-4 of UQCRB in the SCI$_1$-III$_2$IV$_1$ structure, we substituted its position with the AlphaFold
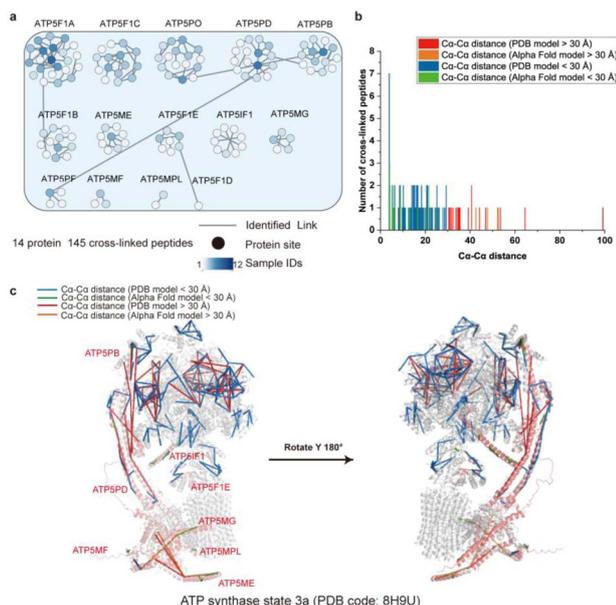
**Fig. 4** Crosslinked peptides of ATP synthase (complex V). (a) Cross-linked peptides involved in the ATP synthase (complex V) were selected from SI Fig. 1 and displayed individually. In the network, nodes represent proteins and lines represent identified crosslinks between them. Node colors indicate the number of samples in which each protein interaction was observed. (b) Histograms showing the length distribution of all distance restraints on the protein structures (from (c)) after docking. (c) The identified crosslinked sites were mapped on the complex V structure (PDB: 8H9U). The AlphaFold model, aligned with complex V, is shown in red (see the Methods section for details), with crosslinks mapped as Cα–Cα distances between subunit residues. Crosslinks within 30 Å are shown in blue (PDB) or green (AlphaFold), and those over 30 Å are shown in red (PDB) or orange (AlphaFold).

model of UQCRB. The Cα–Cα distance between Lys-4 of UQCRB and Lys-92 of UQCRC2 was measured at 35.1 Å, suggesting that this crosslinked site was located within a flexible region of CIII (Fig. 3c). Notably, this inter-crosslinked peptide was also identified in HepG2 cells,[9] providing complementary distance constraint information for the cryo-EM structure of the supercomplex $SCI_1III_2IV_1$.

In summary, 160 of 179 crosslinked peptides matched the structures of $SCI_1III_2IV_1$ and complex II, with 96% (154/160) of these peptides exhibiting crosslinked sites compatible with the PDB structure. 19 crosslinked peptides were located in unresolved protein regions, and 15 crosslinked peptides, combined with AlphaFold-predicted structural models, provided additional structural insights into the $SCI_1III_2IV_1$ complex (Fig. 3b). These findings demonstrated that CD-MS effectively crosslinked proteins within the electron transport chain in tumor cells from tumor-bearing mice, offering complementary structural information on mitochondrial protein interactions.

Second, ATP synthase (complex V), embedded in the inner mitochondrial membrane, drives ATP production by catalyzing the final step of OXPHOS. Electrons from oxidized nutrients transfer through complexes I–IV, generating water and the proton motive force (PMF), which ATP synthase utilizes to synthesize ATP from ADP and inorganic phosphate (Pi) *via*

a rotational mechanism. The human monomeric ATP synthase comprises 29 polypeptide chains from 18 different subunits, with a total molecular weight of 592 kDa. Crosslinked peptides were identified and mapped against the cryo-EM structure of human ATP synthase (PDB code: 8H9U).[20] Notably, this cryo-EM structure included only 17 subunits, as the DAPIT subunit was lost during the dissociation process. In total, 145 crosslinked peptides provided structural site information for 14 protein subunits (Fig. 4a), achieving 89% coverage of ATP synthase subunits, including the missing DAPIT subunit. Among these, 122 crosslinked peptide pairs were mapped to the reported ATP synthase structure, with 82% (100/122) conforming to the expected protein structure (Cα–Cα distance < 30 Å). Some crosslinked peptides, however, exceeded the theoretical cross-linked arm length (Cα–Cα distance > 30 Å), likely due to the inherent dynamic conformational changes of these subunits *in vivo* (Fig. 4b).

Of the 145 identified crosslinked peptides, 23 were located in unresolved regions across 10 ATP synthase subunits, all of which were positioned within the dynamic rotational domain of the enzyme (Fig. 4c). These included the β (ATP5PB) subunit in the F1 domain, several subunits in the Fo domain—ATP8 (MT-ATP8), e (ATP5ME), f (ATP5MF), g (ATP5MG), DAPIT (ATP5MD), and 6.8 PL (ATP5MJ)—as well as the ε (ATP5F1E) subunit within the "rotor" domain, which connects the F1 and Fo domains. Additionally, the d (ATP5D) and IF1 (ATP5IF1) subunits in the "stator" domain were identified. Importantly, 4 crosslinked peptides provided structural information on the missing DAPIT subunit, demonstrating that CD-MS can capture proteins typically lost in the purified structures. Furthermore, compared with the structure predicted by AlphaFold, 87% (20/23) of the crosslinked peptides identified in unresolved regions were found to be compatible with the AlphaFold model. The structural matching rate of ATP synthase decreased from 97% (67/69) in cultured HepG2 cells (previously identified)[9] to 83% (120/145) in animal models (this study), which may reflect the rotational state of ATP synthase during proton translocation and thus a reduced matching efficiency *in vivo*. This highlights the potential of CD-MS for revealing dynamic structural insights beyond those captured in static structural models.

Third, the identified thermogenic metabolic proteins include auxiliary proteins involved in OXPHOS complex assembly, such as carnitine *O*-palmitoyltransferases (CPT1A and CPT1B) and long-chain fatty acid-CoA ligase (ACSL1) for fatty acid metabolism, as well as adenylate cyclase 10 (ADCY10) and cAMP-dependent protein kinase alpha catalytic subunit (PRKACa) for signal transduction. A total of 29 crosslinked peptides were identified across 18 thermogenic metabolism-related proteins (SI Fig. 6a). Among these, 18 crosslinked peptides from 13 proteins lacking resolved structures were analyzed using AlphaFold-predicted models. In addition, two crosslinked peptides involving NADH dehydrogenase (ubiquinone) complex I assembly factor 7 (NDUFAF7) and NADH dehydrogenase (ubiquinone) 1α subcomplex assembly factor 2 (NDUFAF2) could not be evaluated because no AlphaFold models were available. Combining these analyses with mapped PDB structural information, 96% of the crosslinked peptides

(26 of 27) were consistent with reported protein models or AlphaFold structures, with Cα–Cα distances below 30 Å (SI Fig. 6b). In summary, as most thermogenic metabolism-related proteins lack resolved structures, including NDUFAF7 and NDUFAF2, which have neither reported nor AlphaFold-predicted structures, the ability of CD-MS to capture cross-linked peptide information highlighted its advantage in analyzing dynamic protein structures.

### Protein conformation and interactome in mitochondrial ribosomal and branched-chain amino acid degradation from HepG2 tumor cells

KEGG pathway analysis of the 654 identified crosslinked proteins also revealed enrichment in mitochondrial ribosomal proteins and branched-chain amino acid (BCAA; leucine, isoleucine, and valine) degradation. Mitochondrial ribosomes are essential for synthesizing the 13 mitochondria-encoded OXPHOS subunits, while BCAAs are closely linked to tumor metabolic reprogramming; both pathways are implicated in tumor progression.

The translation of mRNA into proteins is crucial for cell growth and survival and is mediated by large and small ribosomal subunits with the mRNA, assisted by eukaryotic initiation factors (eIFs) and elongation factors (eEFs) to ensure both speed and accuracy.[21] 91 crosslinked peptides were identified in 43 protein subunits of the large and small mitochondrial ribosomal complexes (Fig. 5a), with their biological pathways illustrated in SI Fig. 8. Based on the 2.2 Å resolution structure of the human mitochondrial ribosome reported by Singh et al.,[22] 76 crosslinked peptides were mapped onto the mitochondrial ribosome complex. As depicted in Fig. 5b, 95% (73 out of 76) of these peptides align well with the ribosome structure. Among them, 15 crosslinked peptides were located in the unresolved regions of six protein subunits (MRS28, MRS31, MRPL48, MRPL50, MRPL12, and MRPL52). Then, the crosslinked peptides mapped to AlphaFold-predicted structures were integrated into the cryo-EM model (PDB:7QI4), providing more complete structural information.

Overall, as shown in Fig. 5b and c, 97% of the crosslinked peptides (88 out of 91) aligned with either the protein structure or AlphaFold models, with a Cα–Cα distance of less than 30 Å. These findings demonstrate that CD-MS effectively captured crosslinks within ribosomal proteins in HepG2 tumor cells, providing structural restraints that complement existing cryo-EM data.

BCAAs play a crucial role in tumor cell metabolism, and alterations in BCAA metabolism can significantly impact tumor progression.[23] For example, branched-chain amino acid trans-aminases 1 and 2 (BCAT1 and BCAT2) catalyze the reversible conversion of BCAAs into their degradation products, branched-chain α-keto acids (BCKAs). Elevated expression of BCAT1 and BCAT2 has been linked to malignant tumor phenotypes, including enhanced tumor growth and invasion. A total of 105 crosslinked peptides provided structural site information for 27 proteins involved in BCAA metabolism, with their biological functional pathways illustrated in SI Fig. 9. Among these, 26
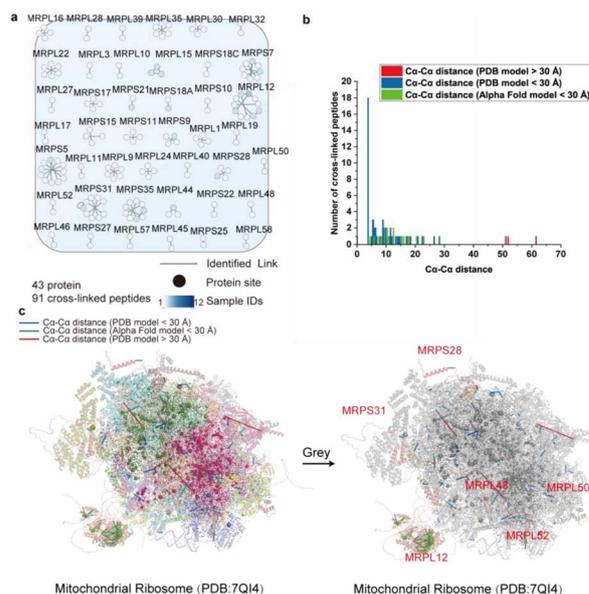


Fig. 5 Crosslinked peptides of mitochondrial ribosomal proteins. (a) Crosslinked peptides involved in mitochondrial ribosomal proteins were selected from SI Fig. 1 and displayed individually. In the network, nodes represent proteins and lines represent identified crosslinks between them. Node colors indicate the number of samples in which each protein interaction was observed. (b) Histograms showing the length distribution of all distance restraints on the protein structures (from (c)) after docking. (c) The identified crosslinked sites were mapped on the mitochondrial ribosomal protein structure (PDB: 7QI4). The AlphaFold model, aligned with mitochondrial ribosomal proteins, is shown in red (see the Methods section for details), with crosslinks mapped as Cα–Cα distances between subunit residues. Crosslinks within 30 Å are shown in blue (PDB) or green (AlphaFold), and those over 30 Å are shown in red (PDB) or orange (AlphaFold).

crosslinked peptide sites were located in previously unresolved protein regions. As shown in SI Fig. 10 and 11, 96% (101 out of 105) of the crosslinked peptides were well-mapped to protein structures or AlphaFold models, with Cα–Cα distances of less than 30 Å, further enhancing our understanding of the structural conformation of these metabolic proteins.

## Experimental

### Cell culture

HepG2 human liver carcinoma cells were cultured in Dulbecco's modified Eagle's medium (DMEM). The medium was supplemented with 10% fetal bovine serum (FBS) and 1% penicillin–streptomycin in 5% $CO_2$ at 37 °C in a humidified incubator. HepG2 cells were seeded in a 150 mm Petri dish and grown to 80% confluency prior to implantation in mice.

### In situ cross-linking of mitochondrial protein complexes in tumor-bearing mice

Immunodeficient BALB/c nude mice 4–5 weeks old (Liaoning Changsheng Biotechnology Co., Ltd) were used for all experiments. All animal procedures were performed in accordance with the Guidelines for Care and Use of Laboratory Animals of

the Dalian Institute of Chemical Physics, Chinese Academy of Science and approved by the Animal Ethics Committee of Dalian Institute of Chemical Physics, Chinese Academy of Science. Monolayer cultures of the HepG2 cell lines were dissociated and washed with PBS and then resuspended in serum-free DMEM at a concentration of $1 \times 10^7$ cells per mL. A subcutaneous tumor was generated by injecting $2 \times 10^6$ cells mixed with Matrigel (Corning) into the right rear flank. The size of the tumor was measured in two dimensions with a caliper, and the tumor volume was estimated as $(\text{width})^2(\text{length})/2$. When a tumor had grown to a volume of about 75 mm$^3$, intra-tumoral injections of a 1.8 mg mL$^{-1}$ 70DDAB@PLGA/Kolliphor EL NP solution (in $1\times$ PBS) were started. For the injection step, a total volume of 200 μL of the nanocarriers was injected into three or four sites in the tumor. Six hours after injection, the mice were humanely euthanized, and tumor tissues were aseptically excised and sectioned into 1 mm$^3$ tumor blocks. The tumor samples were washed three times with pre-chilled $1\times$ PBS, excess PBS was removed, and the tumor tissues were subsequently frozen at −80 °C for further analysis.

### Sample preparation of the cross-linked proteins using i-FASP

Tumor tissues were lysed in lysis buffer containing 10% C12Im-Cl and 1% protease inhibitors, followed by sonication at 180 W for 10 min (5 s on, 15 s off) on ice and centrifugation to remove debris at 16 000×g for 20 minutes at 4 °C. Protein concentration in the supernatant was measured using the BCA assay. Proteins were denatured with 100 mM dithiothreitol (DTT) at 95 °C. A total of 150 μg of protein was transferred to a 10 kDa molecular weight cutoff filter (Sartorius, Germany) and centrifuged at 14 000×g for 20 minutes at 25 °C. Alkylation was performed with 20 mM iodoacetamide (IAA) for 30 minutes in the dark, and remaining reagents were removed by repeated washing by 50 mM NH$_4$HCO$_3$. Proteins were then digested with trypsin (1 : 25, w/w) at 37 °C for 15 hours. Peptides were collected by centrifugation, eluted, lyophilized, and stored at −80 °C for mass spectrometry analysis.

### Fractionation of cross-linked peptides using high-pH reversed-phase chromatography

Tryptic peptides (400 μg) were fractionated using high-pH reversed-phase liquid chromatography (RPLC). Briefly, peptides were resuspended in mobile phase A (98% H$_2$O, 2% ACN, pH 10) and loaded onto a Durashell C18 column (5 μm, 100 Å, 4.6 × 200 mm i.d.). Separation was performed on an Agilent Technologies HPLC system at a flow rate of 1 mL min$^{-1}$ using a 70 minute gradient of increasing mobile phase B (2% H$_2$O, 98% ACN, pH 10). The gradient program was as follows: 0% B for 10 min, 0–2% B for 1 second, 2–30% B for 35 min, 30–45% B for 15 min, and 45–90% B for 10 min. The fractionations were collected every 1 minute starting at 10 minutes and combined into 30 pooled fractions (e.g., fraction 1 + 31, fraction 2 + 32, etc.). Each fraction was analyzed in technical triplicate using LC-MS on an Orbitrap Exploris 480 Mass Spectrometer.

### LC-MS/MS analysis

An Easy-nLC 1200 system coupled to an Orbitrap Exploris 480 Mass Spectrometer (Thermo Fisher Scientific, USA) with a FAIMSPro Interface (San Jose, CA) was employed for LC-MS/MS analysis. The samples were automatically loaded onto a C18 capillary column (150 μm i.d. × 30 cm) and then packed in-house with ReproSil-Pur C18-AQ particles (1.9 μm, 120 Å) with low-pH mobile phases (buffer A: 100% H$_2$O + 0.1% FA; buffer B: 20% H$_2$O + 80% ACN + 0.1% FA). For the fractionated cross-linked peptides, the separation gradient was achieved by applying 12–30% B for 45 min, 30–38% B for 6 min, 38–95% B for 4 min, and 95% B for 6 min. The method parameters of the run were as follows: data-dependent acquisition; full MS resolution of 60 000 at $m/z$ 200; scan range of 350–1500; MS1 AGC target of $3 \times 10^6$; MS/MS resolution of 15 000 at $m/z$ 200; MS1 maximum injection time of 20 ms; MS/MS AGC target of $7.5 \times 10^4$; MS/MS maximum injection time of 30 ms, fixed first mass of 110 $m/z$; isolation window of 1.6 $m/z$; higher-energy collision dissociation (HCD) with a normalized collision energy (NCE) of 30; charge exclusion: unassigned 1, 2, >8. Default settings were used for FAIMS with a total carrier gas flow of 4 L min$^{-1}$ and compensation voltages (CV) of −45 V and −65 V. Each fractionation was analyzed three times. The sample concentration was measured using a NANODROP ONE (Thermo Fisher Scientific, USA) to ensure approximately equal loading amounts of each sample.

### Database search

The identification of crosslinks was performed using pLink 2.0 (v2.3.5)[24] with a separate false discovery rate (FDR) threshold of 1% at the spectrum level. Peptide spectra were matched against a database constructed from MitoCarta3.0,[25] which annotates human mitochondrial proteins. The search parameters were defined as follows: precursor mass tolerance of 20 ppm, fragment mass tolerance of 20 ppm, and precursor filter tolerance of 10 ppm. The crosslinker used was DSS, targeting lysine residues (K) and protein N-termini, with a cross-link mass shift of 138.0680796 Da and a mono-link mass shift of 156.0786442 Da. Carbamidomethylation of cysteine (+57.0215 Da) was set as a fixed modification, while methionine oxidation (+15.9949 Da) and protein N-terminal acetylation (+42.0106 Da) were included as variable modifications.

## Conclusions

Given that crosslinkers cannot efficiently traverse multiple biological barriers in complex environments, particularly at the tissue level, we demonstrate the effectiveness of the CD-MS method for *in vivo* crosslinking analysis of mitochondrial protein interactions in HepG2 tumor cells through intratumoral injection of crosslinker-loaded nanoparticles into xenografted mice. We acknowledge the inherent challenges of intratumoral nanoparticle delivery in solid tumors. Our data may therefore predominantly reflect mitochondrial protein interactions from tumour microregions with higher nanoparticle exposure, whereas deeply hypoxic/necrotic or highly fibrotic

compartments may be under-represented if they receive little or no nanoparticle/crosslinker. Nonetheless, within the nanoparticle-accessible fraction we achieved substantial depth. Moreover, the use of immunodeficient BALB/c nude mice for HepG2 xenograft establishment minimizes the infiltration of functional immune cells, and the exclusive annotation and identification of human mitochondrial proteins against the MitoCarta3.0 database effectively exclude the interference of mouse-derived stromal and immune cell mitochondria, thus ensuring that our detected mitochondrial protein signals are predominantly derived from human HepG2 tumor cells. These experimental and data-processing designs collectively enhance the specificity and reliability of our *in vivo* mitochondrial protein complex mapping in tumor-bearing mice. Eventually, using engineered nanoparticles for targeted mitochondrial delivery, we identified 2368 crosslinked peptides from 654 mitochondrial proteins, covering 58% of the human mitochondrial proteome, with protein abundances spanning five orders of magnitude. Importantly, our analysis revealed 217 mitochondrial PPIs, including 146 PPIs not annotated in STRING databases. GOCC analysis indicated that many of these newly identified interactions are associated with mitochondrial organization, translation, and fusion, providing insights into the structural and functional dynamics of mitochondrial protein networks in tumor cells. Notably, we uncovered an interaction between HSPD1 and SND1 that may represent an important contributor to liver disease. In addition, we identified MRPL37 in association with the key fusion regulators OPA1 and MFN2, suggesting that ribosomal subunit proteins may cooperate in mitochondrial fusion.

In our dataset, 58.1% (126/217) of the identified mitochondrial PPIs were assigned to proteins from different mitochondrial subcompartments, whereas 41.9% (91/217) were assigned within the same subcompartment. The relatively high proportion of inter-subcompartment PPIs was likely caused by the fact that mitochondria are highly dynamic organelles rather than static, rigidly separated compartments. They undergo continuous structural remodeling and functional coupling, including metabolite exchange across compartments, formation of transient contact sites between mitochondrial membranes, and coordinated assembly of multi-subunit complexes spanning different subcompartments. Furthermore, mitochondrial gene expression and protein biogenesis also require coordinated interactions among proteins localized to different mitochondrial regions in living tumors.

Additionally, we identified a total of 549 crosslinked peptides in proteins involved in metabolic pathways closely associated with tumor progression. This included 324 peptides from oxidative phosphorylation proteins, including 179 in 46 ETC proteins and 145 in 14 ATP synthase subunits, together with 29 peptides from 18 additional thermogenesis-related proteins. A further 91 peptides were detected in 43 ribosomal subunits and 105 in 27 proteins involved in branched-chain amino acid metabolism. Furthermore, our study resolved conformational information for previously uncharacterized protein regions, including the missing DAPIT subunit of ATP synthase and the domains of several proteins associated with the aforementioned pathways. By integrating crosslinked peptide site information with both AlphaFold-predicted structures and experimentally determined PDB models, we achieved a comprehensive view of protein conformation. The high concordance (92%, 504/549) between the identified crosslinked peptides and the structural data from AlphaFold or the PDB further validates the robustness of this approach. Notably, the structural matching rate of ATP synthase decreased from 97% in cultured HepG2 cells to 83% in animal models, a reduction that may be attributable to its intrinsic rotational dynamics during proton translocation. Overall, this study highlights the power of *in situ* XL-MS for deciphering mitochondrial protein architectures and interactions in complex biological environments, offering a powerful strategy for investigating mitochondrial conformation and interactions in live mice tumors and mitochondrial diseases.

## Author contributions

Kaiguang Yang, Lihua Zhang and Yukui Zhang designed and supervised the research. Yuwan Chen and BaoFu Ma conducted the experiments. Yuwan Chen, Wenxin Fu, Xinwei Li, and Wen Zhou collected and analyzed the MS data. Yuwan Chen, Wenxin Fu, Kaiguang Yang, Zhen Liang and Lihua Zhang wrote the manuscript with contributions from all co-author.

## Conflicts of interest

There are no conflicts to declare.

## Data availability

The mass spectrometry proteomics data have been deposited to the ProteomeXchange Consortium (https://proteomecentral.proteomexchange.org) *via* the iProX partner repository[26,27] with the dataset identifier PXD072438.

Supplementary information (SI) is available. See DOI: https://doi.org/10.1039/d6sc00098c.

## Acknowledgements

## References

1 M. Momcilovic, A. Jones, S. T. Bailey, C. M. Waldmann, R. Li, J. T. Lee, G. Abdelhady, A. Gomez, T. Holloway, E. Schmid, D. Stout, M. C. Fishbein, L. Stiles, D. V. Dabir,

S. M. Dubinett, H. Christofk, O. Shirihai, C. M. Koehler, S. Sadeghi and D. B. Shackelford, *Nature*, 2019, **575**, 380–384.

2 M. Kim, J. Park, M. Bouhaddou, K. Kim, A. Rojc, M. Modak, M. Soucheray, M. J. McGregor, P. O'Leary, D. Wolf, E. Stevenson, T. K. Foo, D. Mitchell, K. A. Herrington, D. P. Munoz, B. Tutuncuoglu, K. H. Chen, F. Zheng, J. F. Kreisberg, M. E. Diolaiti, J. D. Gordan, J. P. Coppe, D. L. Swaney, B. Xia, L. van 't Veer, A. Ashworth, T. Ideker and N. J. Krogan, *Science*, 2021, **374**, eabf3066.

3 Y. J. Huang, D. Hang, L. J. Lu, L. Tong, M. B. Gerstein and G. T. Montelione, *Mol. Cell. Proteomics*, 2008, **7**, 2048–2060.

4 P. Zhou, D. R. Shaffer, D. A. Alvarez Arias, Y. Nakazaki, W. Pos, A. J. Torres, V. Cremasco, S. K. Dougan, G. S. Cowley, K. Elpek, J. Brogdon, J. Lamb, S. J. Turley, H. L. Ploegh, D. E. Root, J. C. Love, G. Dranoff, N. Hacohen, H. Cantor and K. W. Wucherpfennig, *Nature*, 2014, **506**, 52–57.

5 D. K. Schweppe, J. D. Chavez, C. F. Lee, A. Caudal, S. E. Kruse, R. Stuppard, D. J. Marcinek, G. S. Shadel, R. Tian and J. E. Bruce, *Proc. Natl. Acad. Sci. U. S. A.*, 2017, **114**, 1732–1737.

6 F. Liu, P. Lossl, B. M. Rabbitts, R. S. Balaban and A. J. R. Heck, *Mol. Cell. Proteomics*, 2018, **17**, 216–232.

7 P. S. J. Ryl, M. Bohlke-Schneider, S. Lenz, L. Fischer, L. Budzinski, M. Stuiver, M. M. L. Mendes, L. Sinn, F. J. O'Reilly and J. Rappsilber, *J. Proteome Res.*, 2020, **19**, 327–336.

8 A. Linden, M. Deckers, I. Parfentev, R. Pflanz, B. Homberg, P. Neumann, R. Ficner, P. Rehling and H. Urlaub, *Mol. Cell. Proteomics*, 2020, **19**, 1161–1178.

9 Y. Chen, W. Zhou, Y. Xia, W. Zhang, Q. Zhao, X. Li, H. Gao, Z. Liang, G. Ma, K. Yang, L. Zhang and Y. Zhang, *Nat. Commun.*, 2023, **14**, 3882.

10 W. Zhou, Y. Chen, W. Fu, X. Li, Y. Xia, Q. Zhao, B. Zhao, Y. Zhang, K. Yang and L. Zhang, *Adv. Sci.*, 2024, **11**, e2408462.

11 S. Acharya and S. K. Sahoo, *Adv. Drug Delivery Rev.*, 2011, **63**, 170–183.

12 F. Fang, Q. Zhao, H. Chu, M. Liu, B. Zhao, Z. Liang, L. Zhang, G. Li, L. Wang, J. Qin and Y. Zhang, *Mol. Cell. Proteomics*, 2020, **19**, 1724–1737.

13 J. R. Wisniewski, A. Vildhede, A. Noren and P. Artursson, *J. Proteomics*, 2016, **136**, 234–247.

14 D. Szklarczyk, A. L. Gable, D. Lyon, A. Junge, S. Wyder, J. Huerta-Cepas, M. Simonovic, N. T. Doncheva, J. H. Morris, P. Bork, L. J. Jensen and C. V. Mering, *Nucleic Acids Res.*, 2019, **47**, D607–D613.

15 V. Boczonadi and R. Horvath, *Int. J. Biochem. Cell Biol.*, 2014, **48**, 77–84.

16 H. Liu, J. Zhang, S. Wang, Z. Pang, Z. Wang, W. Zhou and M. Wu, *Cancer Epidemiol.*, 2012, **36**, 82–88.

17 A. Chevrollier, J. Cassereau, M. Ferre, J. Alban, V. Desquiret-Dumas, N. Gueguen, P. Amati-Bonneau, V. Procaccio, D. Bonneau and P. Reynier, *Int. J. Biochem. Cell Biol.*, 2012, **44**, 980–988.

18 M. Kanehisa, Y. Sato and M. Kawashima, *Protein Sci.*, 2022, **31**, 47–53.

19 S. Zong, M. Wu, J. Gu, T. Liu, R. Guo and M. Yang, *Cell Res.*, 2018, **28**, 1026–1034.

20 Y. Lai, Y. Zhang, S. Zhou, J. Xu, Z. Du, Z. Feng, L. Yu, Z. Zhao, W. Wang, Y. Tang, X. Yang, L. W. Guddat, F. Liu, Y. Gao, Z. Rao and H. Gong, *Mol. Cell*, 2023, **83**, 2137–2147.e2134.

21 M. Molenaars, G. E. Janssens, E. G. Williams, A. Jongejan, J. Lan, S. Rabot, F. Joly, P. D. Moerland, B. V. Schomakers, M. Lezzerini, Y. J. Liu, M. A. McCormick, B. K. Kennedy, M. van Weeghel, A. H. C. van Kampen, R. Aebersold, A. W. MacInnes and R. H. Houtkooper, *Cell Metab.*, 2020, **31**, 549–563.e547.

22 V. Singh, Y. Itoh, S. Del'Olio, A. Hassan, A. Naschberger, R. K. Flygaard, Y. Nobe, K. Izumikawa, S. Aibara, J. Andréll, P. C. Whitford, A. Barrientos, M. Taoka and A. Amunts, *bioRxiv*, 2023, preprint, DOI: 10.1101/2023.05.24.542018.

23 L. Qian, N. Li, X.-C. Lu, M. Xu, Y. Liu, K. Li, Y. Zhang, K. Hu, Y.-T. Qi, J. Yao, Y.-L. Wu, W. Wen, S. Huang, Z.-J. Chen, M. Yin and Q.-Y. Lei, *Nat. Metab.*, 2023, **5**, 1159–1173.

24 Z. L. Chen, J. M. Meng, Y. Cao, J. L. Yin, R. Q. Fang, S. B. Fan, C. Liu, W. F. Zeng, Y. H. Ding, D. Tan, L. Wu, W. J. Zhou, H. Chi, R. X. Sun, M. Q. Dong and S. M. He, *Nat. Commun.*, 2019, **10**, 3404.

25 S. Rath, R. Sharma, R. Gupta, T. Ast, C. Chan, T. J. Durham, R. P. Goodman, Z. Grabarek, M. E. Haas, W. H. W. Hung, P. R. Joshi, A. A. Jourdain, S. H. Kim, A. V. Kotrys, S. S. Lam, J. G. McCoy, J. D. Meisel, M. Miranda, A. Panda, A. Patgiri, R. Rogers, S. Sadre, H. Shah, O. S. Skinner, T. L. To, M. A. Walker, H. Wang, P. S. Ward, J. Wengrod, C. C. Yuan, S. E. Calvo and V. K. Mootha, *Nucleic Acids Res.*, 2021, **49**, D1541–D1547.

26 T. Chen, J. Ma, Y. Liu, Z. Chen, N. Xiao, Y. Lu, Y. Fu, C. Yang, M. Li, S. Wu, X. Wang, D. Li, F. He, H. Hermjakob and Y. Zhu, *Nucleic Acids Res.*, 2022, **50**, D1522–D1527.

27 J. Ma, T. Chen, S. Wu, C. Yang, M. Bai, K. Shu, K. Li, G. Zhang, Z. Jin, F. He, H. Hermjakob and Y. Zhu, *Nucleic Acids Res.*, 2019, **47**, D1211–D1217.